Influence of Natural External Forcings on Interdecadal Variation of Global Land Monsoon over the Last Millennium in CESM-LME

Zhiyuan Wang, Laurent Z. X. Li, Xiaoyi Shi, Jianglin Wang, Jia Jia

Influence of Natural External Forcings on Interdecadal Variation of Global Land Monsoon over the Last Millennium in CESM-LME

ZHIYUAN WANG,[a,b] LAURENT Z. X. LI,[b] XIAOYI SHI,[a] JIANGLIN WANG,[c] AND JIA JIA[a]

[a] College of Geography and Environmental Science, Zhejiang Normal University, Jinhua, China
[b] Laboratoire de Météorologie Dynamique, IPSL, Sorbonne Université, CNRS, Paris, France
[c] Key Laboratory of Desert and Desertification, Northwest Institute of Eco-Environment and Resources, Chinese Academy of Sciences, Lanzhou, China

(Manuscript received 24 July 2023, in final form 23 April 2024, accepted 3 May 2024)

ABSTRACT: Interdecadal variations of the global land monsoon have been previously attributed to internal fluctuations of the climate system, but the role of natural external forcings was underexplored. Here, we investigate this issue by using the Community Earth System Model ensemble simulations over the last millennium (LM) (AD 950–1850). Our analysis reveals that the surface temperature, with two dominant structures (global cooling/warming and longitudinal sea surface temperature gradient in the tropical Pacific, which affects the Walker circulation), predominantly shapes the leading forced mode of the global land monsoon. This mode, representing 19% of the total variance, manifests as consistent features across South Asia, the southern part of East Asia, North Australia, South America, and western South Africa, contrasting with other monsoon regions. Under global cooling conditions, the monsoon intensity is enhanced in the northern parts of the East Asian and eastern parts of the North and South African monsoons, but it decreases in the other monsoon regions. Under weak Walker circulation conditions, changes in atmospheric circulation in response to the sea surface temperature gradient in the tropical Pacific are associated with a substantial attenuation of almost all land monsoon regions. It was further shown that the global mean surface temperature and the tropical Pacific temperature gradient jointly account for 75% of the total variance in the leading mode of the global land monsoon, with 29% and 46% as their respective contributions. Furthermore, our results suggest that volcanic eruptions are the dominant external forcing for these variations. These findings provide valuable insights for future research on global monsoon dynamics.

SIGNIFICANCE STATEMENT: Our study using the Community Earth System Model reveals that surface temperature significantly impacts decadal global land monsoon (GLM) variations during the last millennium. Two key factors in relation to global-scale cooling/warming and changes in the tropical Pacific sea surface temperature gradient affect the GLM's leading forced mode. The leading forced GLM features remain consistent across regions like South Asia, southern East Asia, North Australia, South America, and western South Africa. Under global cooling, monsoon intensities in most land monsoon regions are enhanced, while they are reduced in northern East Asian land monsoon regions. In contrast, weak tropical Pacific temperature gradient conditions cause a decrease in intensities in almost all land monsoon regions. Additionally, the global mean surface temperature and the tropical Pacific temperature gradient account for 75% of the total variance in the leading forced GLM variations, contributing 29% and 46%, respectively. Notably, volcanic eruptions emerge as the key external factor influencing these variations.

KEYWORDS: Volcanoes; Monsoons; Climate models; Interdecadal variability

1. Introduction

The global monsoon, an important feature of Earth's climate, comprises a few regional components, such as the Asian, Australian, African, and American monsoons. They are all marked by substantial seasonal alternation in rainfall and atmospheric circulation (Trenberth et al. 2000). Changes in their timing and geographic distribution can have profound impacts on freshwater resources and affect the livelihoods of over two-thirds of the world's population.

Multiple factors influence the monsoon intensity at both global and regional scales. Previous studies suggested that the current global warming has led to discernible anthropogenic changes in global monsoon (Hsu et al. 2012; Wang et al. 2012; Polson et al. 2014). Most of them predicted a significant future intensification due to increased anthropogenic forcing (Hsu et al. 2013; Kitoh et al. 2013; Lee and Wang 2014; Chen et al. 2020; Wang et al. 2020). However, there are also nuanced or even contradicted results in the literature. For example, Zhang and Zhou (2011) found that global land monsoon (GLM) intensity increased during the first half of the twentieth century but experienced a weakening trend until the 2000s. Wang and Ding (2006) also reported that there was no significant trend in global land monsoon intensity since 1980, despite the rapid increase in global mean surface temperature (GMST). These contrasted studies indicate the important role of climate's natural variability that could strongly modulate the monsoon trend under global warming. Actually, significant

Supplemental information related to this paper is available at the Journals Online website: https://doi.org/10.1175/JCLI-D-23-0443.s1.

Corresponding authors: Zhiyuan Wang, wzhy@zjnu.edu.cn; Laurent Z. X. Li, laurent.li@lmd.ipsl.fr

DOI: 10.1175/JCLI-D-23-0443.1

and independent correlations were found between the Northern Hemisphere summer monsoon intensity and the Atlantic multidecadal oscillation (AMO), as well as mega-El Niño–Southern Oscillation (ENSO), on interdecadal time scales (Wang et al. 2013). It was even reported that global precipitation variation seems more responsive to natural external forcings, such as solar irradiation and volcanic eruptions, on decadal time scales than to anthropogenic forcing (Liu et al. 2012, 2013). Discerning the response of global monsoon to natural and anthropogenic signals remains a challenge for the scientific community. Still, it has tremendous theoretical and practical implications for understanding anthropogenic climate change.

The last millennium (LM) is a crucial period for paleoclimate research. It provides valuable insights into the evolution of Earth's climate for its recent past and is helpful to contextualize the current period of anthropogenic warming. Several studies suggest that external natural forcings strongly influenced the global monsoon during the last millennium on multidecadal to centennial time scales (Liu et al. 2009, 2012; Wang et al. 2021). Specifically, the primary mode of global summer monsoon precipitation variations at these time scales is a forced response to external natural forcing with a global pattern (Liu et al. 2012), associated with increased land–ocean thermal contrast and enhancement of the east–west sea surface temperature contrast over the tropical Pacific Ocean (Zuo et al. 2021). Despite numerous studies seeking multidecadal variations in global monsoon, most findings have been primarily based on single-member simulations driven by mixed external forcings (e.g., Liu et al. 2012; Wang et al. 2021). However, identifying climate signals in precipitation proves more complex than in surface temperature (Deser et al. 2012, 2014), even in the configuration of multimember simulations if only the simple ensemble mean is used (Wang et al. 2023). This complexity arises because regional precipitation does not exhibit high sensitivity to external forcings. Consequently, it is a difficult task to correctly determine the primary external forcing responsible for the interdecadal global monsoon variability, as well as the underlying physical mechanisms over the last millennium.

This study utilizes a dataset of large-size ensemble simulations performed by a state-of-the-art climate model and advanced statistical methods to address key questions on the primary role of external natural forcing in driving interdecadal global land monsoon variability over the last millennium (AD 950–1850). Specifically, we aim to identify the primary forced GLM variation at interdecadal time scales over the last millennium and to elucidate its influence mechanisms. The subsequent section offers a detailed overview of the datasets and methodologies employed in this study. Section 3 presents the leading GLM variation driven by external natural forcing. We disentangle and explore forced GLM under different temperature conditions, quantify their contributions, and determine the dominant external forcing to the leading mode of GLM over the last millennium. Finally, section 4 summarizes the key findings and suggests a few potential directions for future research.

2. Methods and data

a. Model data

This study relies on model data from the Community Earth System Model-Last Millennium Ensemble (CESM-LME). CESM (version 1.1) is a coupled model integrating the Community Atmosphere Model, version 5 (CAM5); the Community Land Model, version 4 (CLM4); and the Parallel Ocean Program, version 2 (POP2). CAM5 and CLM4 have a horizontal resolution of 2.5° × 1.875°, while the POP2 grid consists of 320 grids in longitude and 384 in latitude, with an enhanced refinement in the tropics. Twelve ensemble members are used, covering the last millennium (AD 950–1850). They were realized under the same conditions of external forcing, namely, insolation, volcanic eruptions, land-use and land-cover change, greenhouse gases, and orbital forcing, but with small perturbations of air temperature at their initial state. More information about the experimental design can be found in Kay et al. (2015) and Otto-Bliesner et al. (2016). Besides the 12 all-forcing runs (ALLRs), the protocol CESM-LME also performed simulations with individual forcings: GHGR with greenhouse gas only (three members), VOLR with volcanic eruptions only (five members), LUCCR with land-use and land-cover changes only (three members), TSIR with total solar irradiation only (four members), and ORB with orbital parameter change only (three members). CESM-LME was finally completed by a control (CTRL) simulation of 1155 model years, with all external forcing prescribed at AD 850.

Previous studies have demonstrated that CESM-LME experiments can reasonably reproduce the observed characteristics of internal variabilities and responses to external forcings over the last millennium (Otto-Bliesner et al. 2016). Furthermore, data from CESM-LME were also used in numerous studies for climate change over the last millennium (e.g., Zuo et al. 2021, 2023; Chen et al. 2022; Xue et al. 2023), which enhances our confidence in CESM-LME.

b. Definition of the global land monsoon domain

The definition of the GLM region, as proposed by Liu et al. (2012), relies on two criteria: the annual precipitation range (local summer mean minus winter mean) exceeding a threshold of 2.0 mm day^{-1} and the local summer precipitation accounting for more than 55% of the annual total. The local summer is defined as from May through September for the Northern Hemisphere (NH) and from November through next March for the Southern Hemisphere (SH).

A few monsoon strength measurements exist in the literature. They commonly use the local summer (or annual) precipitation or the annual precipitation range. Such monsoon strength metrics, however, may lead to spurious results or even misleading monsoon strength for regions that have abundant rainfall for both summer and winter (Zeng and Zhang 2020) and for the extratropical monsoon areas, in which the annual precipitation range generally decreases with latitude (Wang et al. 2011).

In this study, we use the annual range precipitation normalized by the annual mean precipitation to define monsoon intensity (MI):

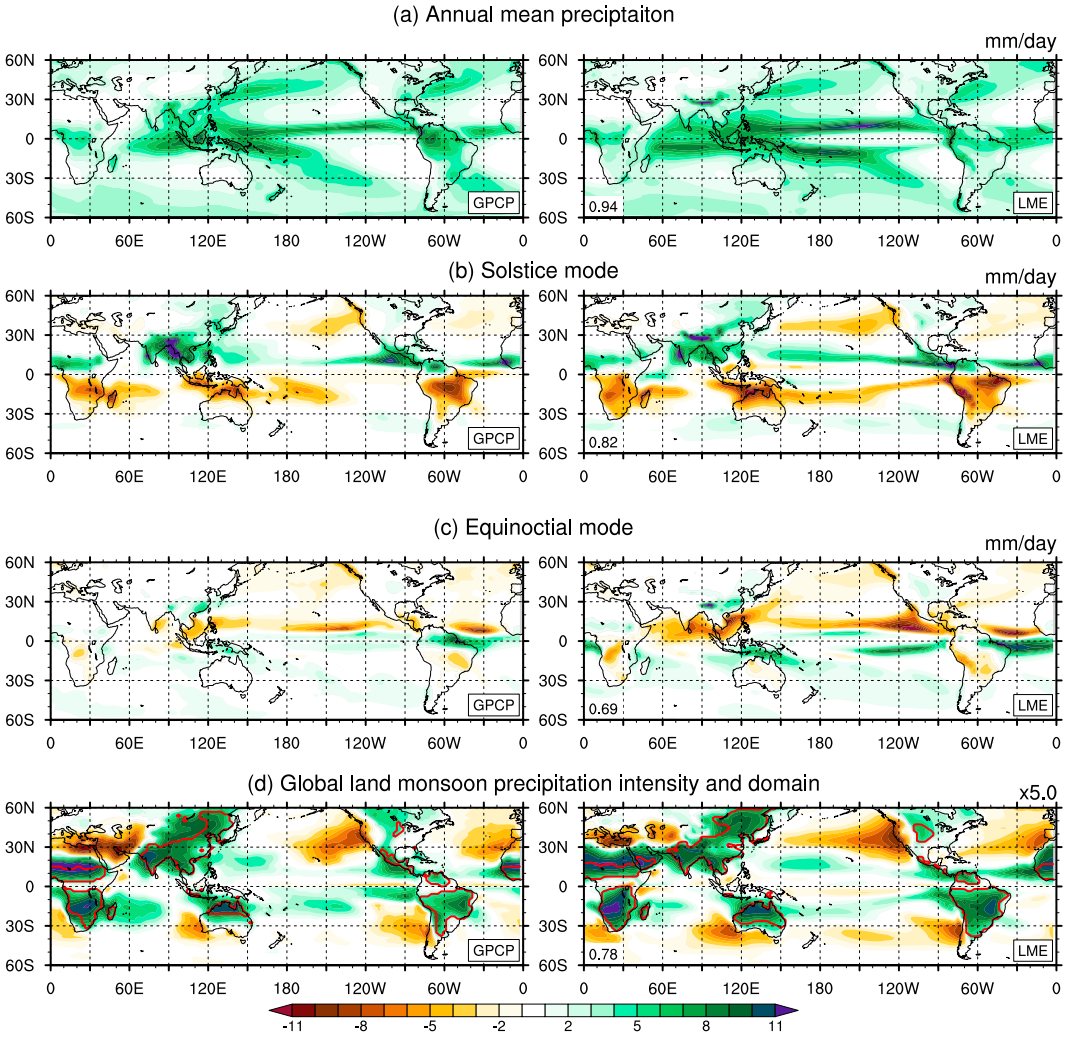

FIG. 1. Precipitation climatology (AD 1979–2005) in (left) GPCP and (right) CESM-LME (12-member ensemble mean in ALLR). (a) Annual mean precipitation (mm day^{-1}), (b) the solstice mode [June–September (JJAS) minus December–March (DJFM)], (c) equinoctial asymmetric mode (AM minus ON), and (d) MI (nondimensional) and GLM domain (outlined by red contours). The monsoon domain is defined as regions where the summer-minus-winter precipitation rate exceeds 2.5 mm day^{-1} and the summer precipitation exceeds 55% of the annual mean amount, with summer being May–September (MJJAS) for the NH and November–March (NDJFM) for the SH. Numbers in the lower left corners indicate the pattern correlation coefficient between GPCP and CESM-LME.

$$\mathrm{MI} = \frac{P_r}{P_m}, \tag{1}$$

where P_r is the difference in total precipitation between the local summer and winter. The term P_m is the annual mean precipitation. Boreal (austral) summer and winter seasons are denoted as May–September (November–next March) and November–next March (May–September), respectively. The normalization allows for comparisons between regions with different levels of total precipitation and provides a comprehensive measure of monsoon intensity. While the annual range captures the degree of precipitation in summer in monsoon regions, dividing it by the annual mean provides a normalized measure of monsoon intensity that considers both the degree of precipitation in summer and the total amount of precipitation throughout the year.

c. *Model evaluation*

As mentioned earlier, many previous works have thoroughly assessed the performance of the simulated precipitation and surface temperature at both global and regional scales within the CESM-LME framework. Given our focus on the GLM intensity, we show here our evaluation of CESM-LME in reproducing three simple metrics in relation to the global monsoon (Wang and Ding 2008): 1) annual mean precipitation, 2) first and second modes of the annual cycle of precipitation, and 3) monsoon intensity and GLM domain.

Figure 1 compares precipitation climatology (AD 1979–2005) between observation [Global Precipitation Climatology Project (GPCP)] (Adler et al. 2003) and CESM-LME's 12-member ensemble mean of the ALLRs. The simulations well reproduce the

main observed features of the annual mean precipitation (Fig. 1a; pattern correlation is 0.94), including the tropical oceanic convergence zones, the precipitation zones in the extratropical Pacific, and the corresponding longitudinal and latitudinal asymmetries in annual mean precipitation. The simulations also simulate the solstice mode (mean precipitation of local summer minus winter) and equinoctial mode [mean precipitation of April–May (AM) minus October–November (ON)] with high fidelity (Figs. 1b,c; pattern correlation coefficients are 0.82 and 0.69, respectively).

However, a few discrepancies persist, particularly the model's underestimation of precipitation during the solstice mode over the South Asian and South American monsoon regions, as well as overestimation during the equinox mode across much of the tropics. A plausible explanation for these deviations is the CESM's partial reproduction of the North Pacific subtropical high's dynamics, which may lead to precipitation biases over the tropical Pacific. This challenge of accurately simulating the North Pacific subtropical high is also reflected in most current global climate models, as indicated by previous studies (He and Zhou 2020; Piao et al. 2023). Additionally, the CESM-LME simulations exhibit the commonly reported double intertropical convergence zone (ITCZ) bias over the tropical Pacific, a trait also observed in many state-of-the-art climate models for Coupled Model Intercomparison Project (CMIP) phases 3, 5, and 6 (Tian and Dong 2020).

Nonetheless, the CESM-LME simulations capture the global monsoon strength and GLM domain realistically (Fig. 1d). The pattern correlation coefficient of GLM strength between the simulation and the observation is 0.78 ($p < 0.05$). In this study, we use the observed GLM domain to analyze the monsoon strength change as in previous studies (e.g., Liu et al. 2009, 2012; Wang et al. 2021; Chen et al. 2020). Monsoon intensity, as defined and calculated according to Eq. (1), is used to measure the monsoon strength in these regions (red lines in Fig. 1d).

d. Low-frequency component analysis

Low-frequency component analysis (LFCA) is a powerful analytical framework for distinguishing intrinsic patterns of climate variability across low-frequency domains. Based on the foundational works of Wills et al. (2018, 2020), our study deploys the LFCA methodology in dissecting the GLM intensity variability.

The first step of LFCA, applied to the data $\mathbf{X}(n, p)$ with n years of annual GLM intensity anomalies across p grids, consists of performing a conventional principal component analysis with empirical orthogonal functions (EOFs) representing the spatial structures. These EOFs, designated as $\boldsymbol{\alpha}_k$, are the eigenvectors of the covariance matrix, with associated eigenvalues σ_k^2:

$$\mathbf{C}\boldsymbol{\alpha}_k = \sigma_k^2 \boldsymbol{\alpha}_k, \tag{2}$$

where $\mathbf{C}$ is the covariance matrix constructed by

$$\mathbf{C} = \frac{1}{n-1}\mathbf{X}^{\mathrm{T}}\mathbf{X}. \tag{3}$$

The second step of LFCA is to identify the foremost N EOFs that maximize the low frequency to total variance ratio r_k within their respective time series $\mathbf{t}_k$, computed as

$$r_k = \frac{\widetilde{\mathbf{t}}_k^{\mathrm{T}}\widetilde{\mathbf{t}}_k}{\mathbf{t}_k^{\mathrm{T}}\mathbf{t}_k}, \tag{4}$$

where $\widetilde{\mathbf{t}}_k$ symbolizes the low-frequency variations obtained through a 10-yr low-pass filter applied to $\mathbf{t}_k$, revealing the interdecadal signals.

The application of this technique yields low-frequency components (LFCs) $\widetilde{\boldsymbol{t}}_k$ and their spatial counterparts, the low-frequency patterns (LFPs) $\mathbf{v}_k$, which are computed via regression of the original dataset against the LFCs:

$$\mathbf{v}_k = \mathbf{X}^{\mathrm{T}}\widetilde{\mathbf{t}}_k. \tag{5}$$

As in the conventional EOF methodology, LFCs describe the temporal evolution of their corresponding spatial patterns (LFPs). The resultant LFCs are orthogonal to one another and ordered by decreasing explained variance, while LFPs lose their orthogonality through the transformation.

In this study, the choice to retain a truncation level of $N = 70$ EOFs, which contains roughly 70% of the total variance, stems from the compromise to encompass significant variances pertinent to our research while mitigating computational complexity. This threshold is substantiated by the seminal research of Wills et al. (2018, 2020) and corroborated through our sensitivity tests with $N = 50$ EOFs, which yielded highly consistent LFPs and LFCs, as evinced by their pattern correlations, with correlation coefficients of 0.97 and 0.92, respectively.

Finally, our analysis is primarily focused on the interdecadal variability of GLM intensity over the last millennium (AD 950–1850), consistent with the scope of our preceding inquiries (Wang et al. 2021, 2023). Without specific notations, we utilize annual averages and process data to a 10-yr Lanczos low-pass filter, isolating components above the decadal scale. Anomalies of GLM intensity are calculated with respect to their mean values across the last millennium. To address the causes of monsoon intensity variation, we utilize the boreal (austral) summer and winter from May to September and from November to the following March, respectively. Conversely, the austral counterparts are defined from November to the following March and from May to September, respectively. Notably, when referencing the local summer or winter, we are alluding to the boreal summer or winter in the NH and the austral summer or winter in the SH, respectively.

3. Results

a. Leading forced mode of GLM

We examine the externally forced mode of the interdecadal GLM variability over the last millennium by applying LFCA to the 12-member ensemble-mean monsoon intensity. We use the simulations under all forcings, noted as ALLR. The leading pattern (LFP1) reveals nonuniform structures (Fig. 2a), with positive and negative values across the GLM areas. LFP1

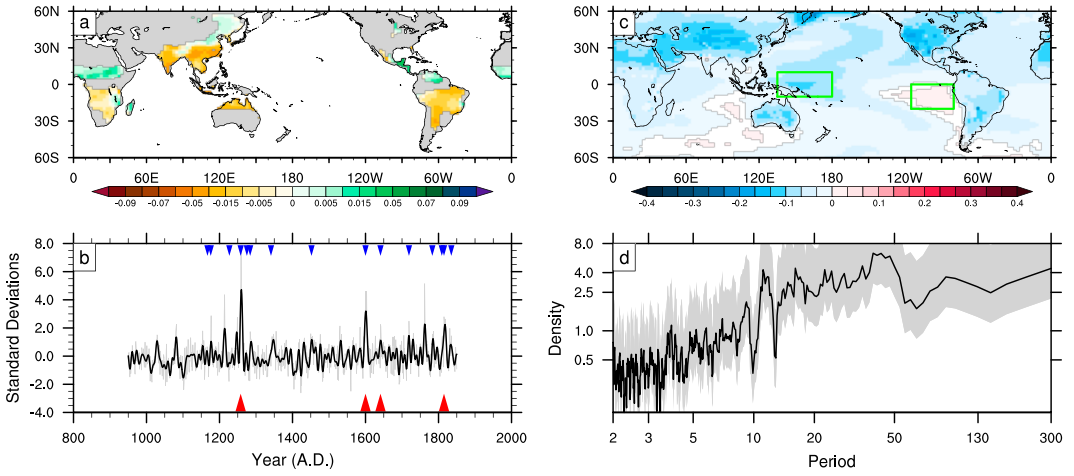

FIG. 2. The leading mode of LFCA applied to GLM intensity. (a) The leading LFP1. (b) The leading LFC1 (thin black); the thick curve is from a 10-yr low-pass filter; blue triangles represent events with the annual stratospheric volcanic sulfate aerosol injection larger than 30 Tg; red triangles represent volcanic events in 1258, 1600, 1641, and 1815, which induced both significant global cooling and western and eastern Pacific contrasts. (c) Surface temperature anomalies (°C) regressed onto LFC1; color shadings represent areas of significance above the 95% confidence level; green boxes in the eastern and western Pacific represent 245°–280°E, 0°–20°S and 135°E–180°, 10°S–10°N, respectively; and (d) the LFC1 spectra (thick line); the gray shadow areas represent the 95% significance range.

explains 19% of the total variance of interdecadal GLM, which is calculated by projecting LFP1 onto the 12 individual members of ALLR over the last millennium. Negative values are found in South Asia, the southern part of East Asia, North Australia, South America, and western South Africa, while positive values are found in the northern part of East Asia, Sahel, and eastern South Africa. This distribution starkly contrasts with the uniform structure of centennial summer monsoon precipitation variations (Liu et al. 2012), which suggests that the monsoon climate might exhibit distinct characteristics over varying time scales.

The significant difference between LFP1 in ALLR and its counterpart in the CTRL run (Fig. S1a in the online supplemental material, with fixed external forcings) suggests that the former may be primarily a response to varying external forcings rather than a consequence of internal variability. Further supporting this assertion is the leading low-frequency component (LFC1; Fig. 2b), which shows large fluctuations concomitant with major volcanic eruptions (Fig. 2b, blue triangles). These fluctuations are statistically distinct from those observed in CTRL (Fig. S1b), especially in the power spectra of LFC1 on decadal and longer time scales, as evidenced by the remarkable peaks shown in Fig. 2d—a remarkable deviation from the reduced power density after approximately 70-yr periods seen in CTRL (Fig. S1d; $p < 0.05$).

The above patterns indicate that LFCA has effectively filtered out the external forcing signals below a decade, and the leading forced mode persists in longer time scales. However, to ascribe the leading mode of GLM in ALLR unequivocally to external forcings, we must consider additional criteria, given that the variations could be attributed to modified variances within the internal modes of GLM variability, e.g., one of the modes by LFCA in CTRL with high explained variance. Hence, elucidating the mechanisms shaping this prominent GLM distribution is imperative.

On the interdecadal time scale, regional precipitation variations are predominantly modulated by atmospheric circulation changes and local sea surface temperature patterns. However, global precipitation cannot be ascribed solely to changes in global mean temperature but is also constrained by the tropospheric energy budget (Allen and Ingram 2002). In the troposphere, the precipitation heating is principally offset by the radiative flux divergence. Consequently, the differential between the radiative flux emitted at the tropopause and that emanating at Earth's surface determines the net global precipitation. All else being constrained, a rise in surface temperature amplifies this flux divergence, leading to increased precipitation. Nevertheless, introducing longwave radiation absorbers into the atmosphere tends to reduce the flux differential, thereby mitigating the increase in precipitation that otherwise occurs with enhanced solar radiation (Allen and Ingram 2002; Liu et al. 2013). Therefore, both GMST and global temperature patterns emerge as key factors in dictating global and regional precipitation distributions. Furthermore, changes in the GLM are mainly linked to anomalous advection of moisture, which is ultimately caused by thermal anomalies in various regions of the globe (Liu et al. 2012; Wang et al. 2014; P. X. Wang et al. 2017).

With the above considerations, our analysis now focuses on delineating the influence of surface temperature changes on the GLM distributions. To this end, we regressed the leading forced mode of GLM (i.e., LFC1) against global surface temperature variations as in previous studies (e.g., Liu et al. 2013; Wang et al. 2013; Wang et al. 2021). Results are shown in Fig. 2c. The surface temperature pattern associated with LFC1 displays a nearly uniform structure on the globe, indicative of

widespread climatic warming or cooling phenomena. The uniformity manifested in the surface temperature might indicate that the leading low-frequency mode of the GLM intensity is not internal variability, which generally creates contrasted patterns across the globe. Previous studies also suggest that the nearly uniform surface temperature or sea surface temperature structure is mainly influenced by external forcings (Liu et al. 2013; Mann et al. 2009; Wang et al. 2021, 2023).

Furthermore, the absence of this uniform temperature pattern in CTRL reinforces our conclusion that external forcings shape the leading mode of GLM variation in ALLR (Fig. S1c). Consequently, we use the term "global cooling" to represent this structure, recognizing the influence of natural external forcings such as volcanism and solar irradiation over the last millennium, which have historically induced a general surface cooling. This cooling pattern is more pronounced over continental regions than over the oceans (Fig. 2c), a finding consistent with multiple model-based studies (e.g., Liu et al. 2012, 2013; Man and Zhou 2014; Wang et al. 2023).

A careful check of the regression map also reveals that the western Pacific warm pool region exhibits more robust cooling compared to other oceanic areas (Fig. 2c, green box regions). Conversely, a significant warming center in the equatorial eastern Pacific (approximately in Niño-1 region) reduces the surface temperature contrast between the equatorial eastern and western Pacific, potentially altering the Walker circulation. These phenomena accord with the existing literature, showing that the alterations in the tropical Pacific sea surface temperature gradients are attributable to natural external forcings (e.g., Liu et al. 2013; Mann et al. 2009). The "ocean dynamical thermostat" theory (Clement et al. 1996; Cane et al. 1997; Bauer et al. 2003) provides an explanation for this phenomenon. This hypothesis argues that reduced radiative forcing is more effective in the western Pacific than in the eastern Pacific, where the weakening upwelling of cold-water masses dampens the temperature change.

b. *Identification and quantification of controlling factors*

It is now clear that two structures of the global surface temperature are tightly related to GLM (particularly its leading mode, LFP1 or LFC1). They are the quasi-uniform surface temperature pattern on the global scale (global cooling) and the latitudinal temperature gradient of the tropical Pacific, respectively. The former can be measured by the GMST, while the latter can be measured by the temperature difference between the western and eastern regions of the tropical Pacific Ocean, a surrogate of the local Walker circulation. Hereafter, we will call the temperature difference the "tropical Pacific temperature gradient" (TPTG). It is to be noted that these two patterns of surface temperature correspond to the first and fourth modes of LFCA when the analysis is applied to the ensemble mean surface temperature of the experiment ALLR (displayed in Fig. S2). We can thus reasonably conclude that the GLM's primary response to external forcing should be a superposition of effects in relation to these two surface temperature patterns. This response is discernible through spatial and temporal analyses.

To independently substantiate our hypothesis, we identify significant historical events defined by notable anomalies in GMST and TPTG. Specifically, we classified events with marked GMST cooling as those exhibiting anomalies below -1.5 standard deviations yet displaying TPTG anomalies within ± 1.0 standard deviations, signifying no substantial weakening or strengthening of the Walker circulation. Conversely, we identified events showing a significant weakening of TPTG, with anomalies below -1.5 standard deviations but without corresponding extreme GMST cooling or warming (anomalies within ± 1.0 standard deviations). As previously mentioned, TPTG is the regional mean surface temperature difference between the western and eastern equatorial Pacific (Fig. 2c, green box regions), representing the zonal surface temperature gradient, a surrogate for the Pacific Walker circulation intensity (e.g., Zinke et al. 2021; Zhao et al. 2022).

From the analysis of CESM-LME ALLR's 12-member ensemble average over the last millennium, we have identified 44 significant cool-GMST-only and 41 significant weak-TPTG-only events across a total of 901 model years. To assess the GLM's intensity response to these two major factors, we composited the GLM intensity response to all significant cool-GMST-only and weak-TPTG-only events. This allows us to ascertain whether there is a consistent GLM distribution in response to the individual and combined effects of GMST cooling and TPTG weakening, further informing our understanding of the GLM distribution's sensitivity to these forcings (e.g., Pausata and Camargo 2019; Zuo et al. 2021).

Figure 3 displays the composite maps of surface temperature and monsoon intensity for cool-GMST-only events, weak-TPTG-only events, and their superposition. As expected, the cool-GMST-only composite exhibits a uniform global cooling pattern but lacks a clear temperature contrast in the eastern and western tropical Pacific (Fig. 3a). This pattern aligns with the influences of natural external forcing on surface temperature, as identified in earlier studies (Mann et al. 2009; Wang et al. 2019, 2022), and is discernibly distinct from patterns driven by internal variability. Additionally, it is worthy of note that the same composite procedure (cool-GMST-only events) applied to CTRL reveals a negative phase of the Pacific decadal oscillation (PDO) pattern (Fig. S3), indicating the crucial role of PDO in the decadal to multidecadal variation of the GMST or NH surface temperature (Steinman et al. 2015; Cheung et al. 2017). This finding confirms that the composite of the cool-GMST-only events reflects surface temperature responses to natural external forcings.

Under weak-TPTG-only conditions, the composite surface temperature pattern demonstrates uniform warming with a cooling center located over the western Pacific warm pool regions, resembling an El Niño–like pattern. This pattern is observed regardless of whether it is derived from ALLR (Fig. 3b) or CTRL (Fig. S3), which implies that external forcing may not significantly alter the El Niño–like pattern but may affect its frequency (discussed in the subsequent section). Notably, the weak-TPTG-only events tend to align with occurrences of GMST warming, with a frequency of 85% in ALLR and 80% in CTRL. This phenomenon is supported by

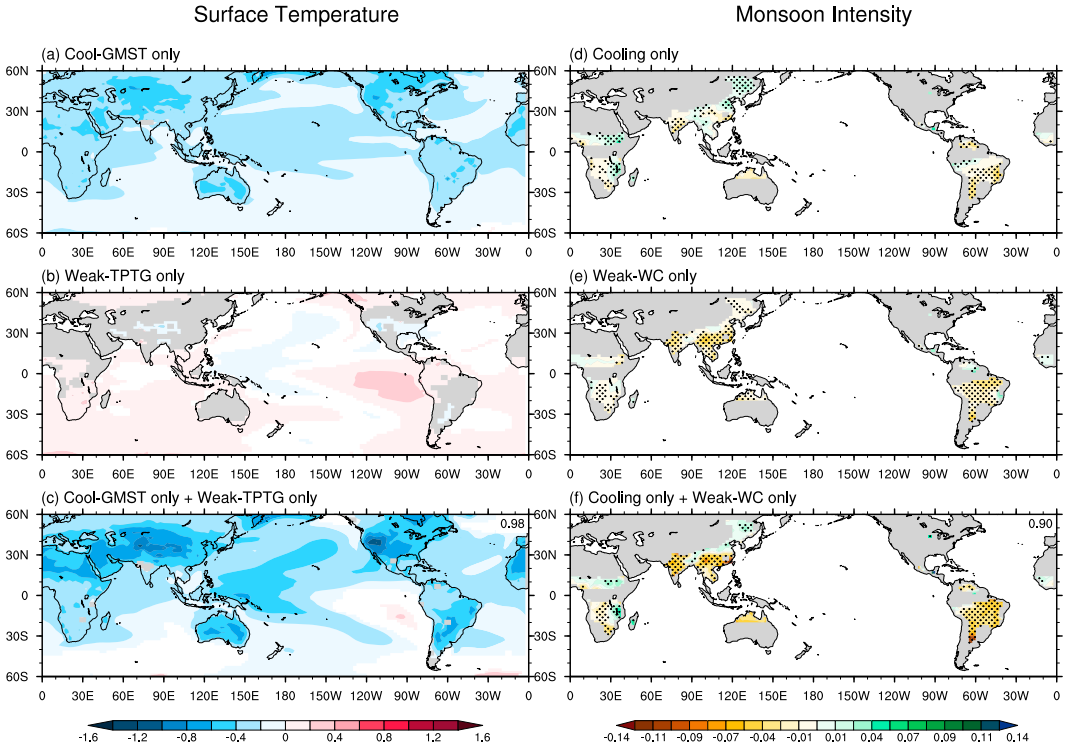

FIG. 3. Composite maps of (left) surface temperature (°C) and (right) GLM intensity (dimensionless) in ALLR. (a),(d) Composite with cool-GMST-only conditions; (b),(e) composite with only cases of weak-TPTG-only conditions; and (c),(f) superimposition of the two precedent cases (cool-GMST only + weak-TPTG only). The figures in the upper-right corners of (c) and (f) indicate the pattern correlation coefficient with the regressed surface temperature (Fig. 2c) and the forced LFP1 (Fig. 2a), respectively. There are 44 cool-GMST-only events and 41 weak-TPTG-only events identified in ALLR. The shading in the maps of surface temperature and the black dots in the maps of MI represent values exceeding the 95% confidence level. GMST and TPTG stand for the global mean surface temperature and tropical Pacific temperature gradient, respectively.

previous studies suggesting that El Niño events may contribute to a rise in GMST (Mann et al. 2017; G. Wang et al. 2017).

Upon combining surface temperature patterns under cool-GMST-only and weak-TPTG-only conditions, we observe a pattern that aligns closely with the regressed surface temperature by the forced LFC1 (Fig. 3c). Similarly, the superposition of the cool-GMST-only and weak-TPTG-only monsoon intensities resembles the forced LFP1 (Fig. 3f). The leading mode of the GLM's forced response can thus be interpreted as a superposition of the two patterns under cool-GMST-only and weak-TPTG-only backgrounds. This synthesis indicates that the leading forced GLM distributions may be simply separated into two externally forced components: global cooling and the weakening of TPTG. We can, therefore, investigate the GLM distributions in response to the two specific external forcing conditions.

The responses of the global monsoon to cool-GMST-only and weak-TPTG-only conditions are presented in Figs. 3d and 3e, respectively. For cool-GMST-only conditions, there is a divergent response in monsoon intensity across geographic sectors, with intensification noted in the northern parts of the East Asian and eastern parts of the North and South African monsoons, contrasted by decreases in the other monsoon regions. These regional responses to cool-GMST conditions are variably distributed across the individual monsoon sectors (refer to Fig. S4 for details). In response to weak-TPTG-only conditions, a generalized weakening of monsoon intensity is observed throughout the monsoonal belts (Fig. 3d), barring minor deviations in the North African and North American monsoon regions. This distribution signifies a more significant contribution of weak-TPTG-only conditions to most individual monsoon intensity changes than cool-GMST-only conditions (additional details in Fig. S4). Such findings highlight the differentiated response of GLM distributions to cool-GMST-only and weak-TPTG-only events, especially within individual monsoon regions.

The response of the monsoon intensity to varying climatic conditions is a complex issue, particularly due to the normalization operation in Eq. (1). Primarily, the monsoon intensity encapsulates the annual precipitation range—defined as the difference between local summer and winter precipitation—and is a crucial metric for characterizing monsoonal behavior (e.g., Wang et al. 2011, 2020; Liu et al. 2016). This differs from climatological metrics such as the annual mean precipitation. Moreover, the distribution patterns of the annual precipitation ranges align closely with those of the GLM intensity

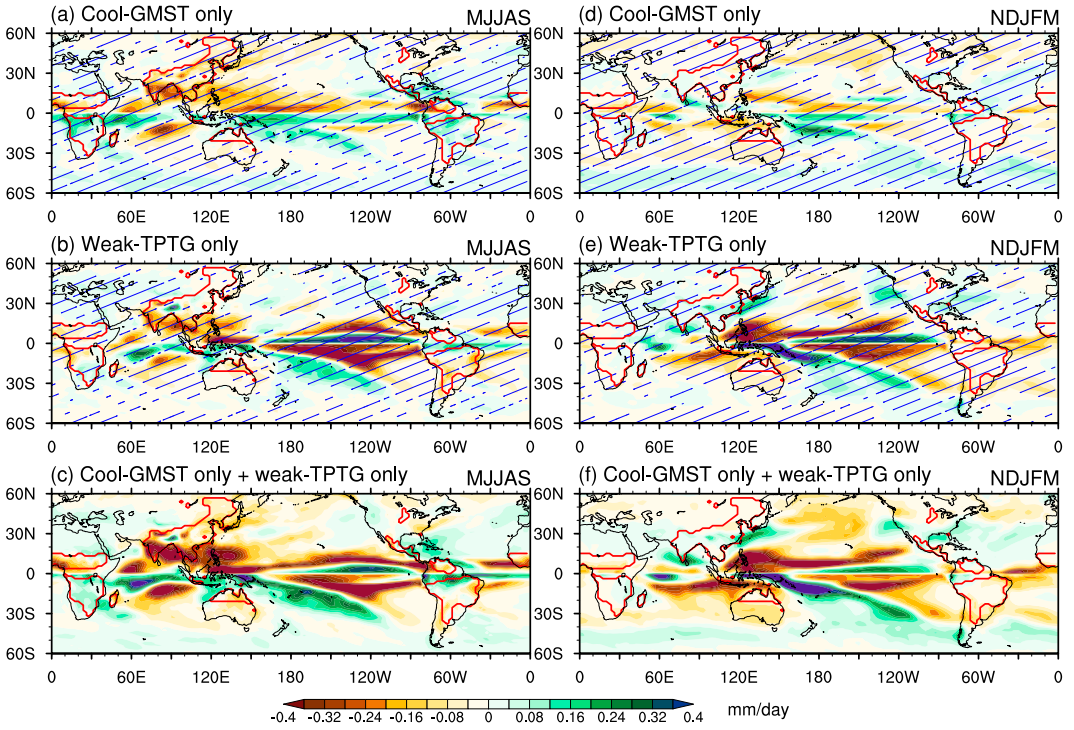

FIG. 4. Composite maps of (left) summer and (right) winter precipitation distributions (mm day^{-1}) in ALLR. (a),(d) Composite with cool-GMST-only conditions; (b),(e) composite with only cases of weak-TPTG-only conditions; and (c),(f) superimposition of the two precedent cases (cool-GMST only + weak-TPTG only). There are 44 cool-GMST-only events and 41 weak-TPTG-only events identified in ALLR. Blue slashes represent values exceeding the 95% confidence level.

(Fig. S5). Therefore, by investigating changes in seasonal precipitation, we can approximately elucidate any possible underlying mechanisms driving changes in monsoon intensity.

Figure 4 shows the summer and winter precipitation distributions under the cool-GMST-only conditions (Figs. 4a,d), weak-TPTG-only conditions (Figs. 4b,e), and their superimpositions (Figs. 4c,f). Under the cool-GMST-only conditions, almost all dampening precipitation in most land monsoon regions occurs during the local summer, while there is a robust increase in precipitation across most monsoon regions during the local winter. These align with the hydrological responses of the climate to aerosol-induced cooling reported in different climate models (Williams et al. 2001; Rotstayn and Lohmann 2002). Global cooling elicits a pronounced pattern of decreased humidity during both summer and winter seasons (refer to Fig. S6 for details), closely paralleling the surface temperature fluctuations (Fig. 3a), reinforcing the hypothesis that global cooling modulates climate toward a "warmer-get-wetter" pattern as identified by Huang et al. (2013).

Under weak-TPTG-only conditions, a decline in the annual precipitation range is observed across most tropical monsoon regions (Fig. S5b), aligning with the modulation of yearly monsoon precipitation by ENSO as documented in observations (International Research Institute for Climate and Society; https://iri.columbia.edu/our-expertise/climate/enso/). CESM-LME successfully captures this observed feature between ENSO variability and monsoon precipitation. The seasonal precipitation in most land monsoon regions exhibits similar spatial distributions (Figs. 4b,d), except for the Asian land monsoon regions, indicating the potential predominance of ENSO-like conditions governing yearly land monsoon precipitation. Many studies have investigated the interplay between ENSO phases and monsoon strength (e.g., Webster and Yang 1992; Liu et al. 2016; Wang et al. 2003, 2013; Zuo et al. 2019, 2021).

The observed reductions in local summer precipitation under the combined influences of cool-GMST and weak-TPTG conditions are nearly ubiquitous across the global land monsoon regions (Figs. 4e,f). This phenomenon aligns with findings from previous studies, notably the patterns induced by NH volcanic eruptions under El Niño–like sea surface temperature (SST) conditions (e.g., Zuo et al. 2021). Both radiative forcing and the SST configuration are pivotal in driving the variations observed in monsoon precipitation. During the local winter season, precipitation decreases across most monsoonal regions, with notable exceptions in the South African and southern Asian monsoon areas. In South Africa, the increase in winter monsoon precipitation is primarily attributed to the overarching global cooling effect. Conversely, in southern Asian monsoon areas, the rise in winter precipitation predominantly arises from the impacts associated with the TPTG pattern.

It is clear that the joint influence of GMST and TPTG shapes the spatial pattern of the leading forced GLM intensity and the corresponding seasonal precipitation variabilities. We

now extend the investigation to the evolution of LFC1 in relation to GMST and TPTG at interdecadal time scales. The temporal correlation coefficients of forced LFC1 with GMST and TPTG are −0.60 and −0.77, respectively ($p < 0.05$). Conversely, in CTRL, there is no significant correlation between LFC1 and GMST ($r = -0.06$), but a strong relationship is observed between LFC1 and TPTG ($r = -0.75$, $p < 0.05$). These findings reinforce our confidence in the dominant role of external forcing in the leading mode of GLM variation. Furthermore, TPTG variation appears to be a significant determinant for the leading mode of GLM variation, regardless of the transient external forcings exerted in the simulation. It aligns with previous research (Wang et al. 2013), which demonstrates that the intensification of NH monsoon is primarily attributable to the interdecadal variation of ENSO. This leads us to an intriguing question: What are the driving forces behind TPTG variation? Are they due to external forcing or internal variability?

To address this question, we examine the relationship between TPTG and GMST in both ALLR and CTRL. Figure 5a displays the correlation coefficient between TPTG and GMST in different configurations over the last millennium. The counterpart during the Little Ice Age (LIA; AD 1350–1850) is plotted in Fig. 5b. We first examine the case of the last millennium (Fig. 5a). In CTRL, the correlation coefficient is modest but significantly negative at the 95% confidence level (Fig. 5a, large red dot). This negative correlation in CTRL reveals that TPTG and GMST are related together through internal processes or feedback from the climate system, but they vary oppositely. Meanwhile, no significant correlation is observed for each individual member of ALLR (Fig. 5a, small blue dots). This implies that the negative correlation between GMST and TPTG in CTRL is neutralized by a positive correlation imposed by the external forcing present in ALLR. This reasoning can be easily proved if we use TPTG and GMST from different members of ALLR, producing a significantly positive correlation coefficient, as shown in Fig. 5 (small gray dots). Actually, such a configuration with TPTG and GMST from different members of ALLR leads to the loss of internal coherence between TPTG and GMST but conserves the signal from the same external forcing. Therefore, the external forcing is detected, although the forced TPTG cannot be easily isolated from other signals or noises (Wills et al. 2020). After removing most of the noise by the ensemble mean of ALLR's 12 members, a significant positive correlation coefficient between GMST and TPTG is observed (Fig. 5, large blue dots), indicating that the external forcing significantly affects the TPTG variation over the last millennium. Moreover, the relationship between GMST and TPTG is more robust during the LIA (Fig. 5b), which experiences strong external forcing variations during the last millennium (e.g., Crowley 2000; Robock 2000; Miller et al. 2012). Thus, while the TPTG index is highly correlated with LFC1 in ALLR and CTRL, the underlying mechanisms appear to differ.

The combined influence of GMST and TPTG over the last millennium is furthermore quantified through a multivariate regression model (≈0.41 × GMST + 0.65 × TPTG). The correlation coefficient of the regression time series and the forced LFC1 stands at 0.87. This regression model accounts for 75% of the total variance of the forced LFC1 with the 12-member ensemble mean of ALLR (all variables are normalized by their own standard deviation), with GMST and TPTG contributing 29% and 46%, respectively. These findings align with previous studies based on various simulated or observed datasets (e.g., Wang et al. 2012, 2013; Liu et al. 2013). These studies suggest that the temperature contrast between the tropical western and eastern Pacific impacts GLM more effectively than other external forcing factors at interdecadal time scales.

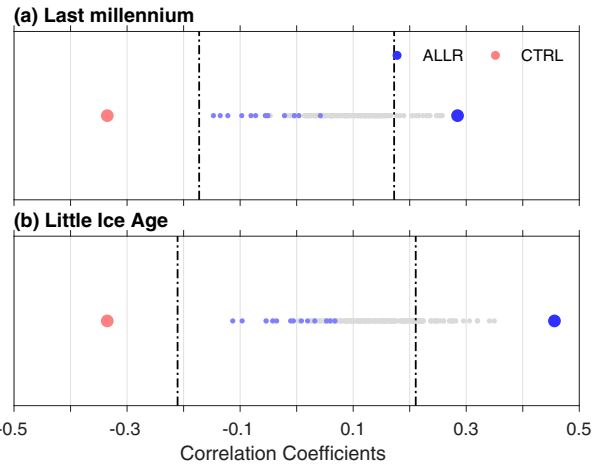

FIG. 5. Correlation coefficients between the TPTG (a surrogate of the local Walker circulation) and GMST from ALLR (blue and gray dots) and CTRL (red dots) during the (a) LM (AD 950–1850) and (b) LIA (AD 1350–1850). Large blue dots denote the ensemble mean of the 12 members from ALLR. Small blue dots denote correlation coefficients of TPTG and GMST in the same individual member of ALLR. Gray dots denote the correlation coefficients of TPTG and GMST across various members. The dashed lines represent the 95% confidence level using a two-tailed Student's *t* test.

c. *Attribution to external forcings*

To identify the dominant external forcing that drives the GLM variation over the last millennium, we examine the linkages between LFC1 derived from ALLR and GMST derived from various sensitivity experiments in CESM-LME. These experiments include only individual external forcings. Each sensitivity experiment consists of more than three individual members described in section 2a, allowing the use of ensemble averaging to isolate the major influence of external forcings on GMST (Hegerl et al. 2011; Wills et al. 2020). Our results show that the correlation coefficients are generally insignificant between the forced LFC1 in ALLR and GMST from each of the sensitivity experiments, except the volcanic eruption sensitivity run (VOLR), which gives a significant negative correlation ($r = -0.61$, $p < 0.05$). This suggests that volcanic eruptions could be the dominant factor influencing the primary forced mode of the GLM variation.

Figure 6a shows the squared coherences between the two time series, GMST and LFC1. The effect of GMST in ALLR

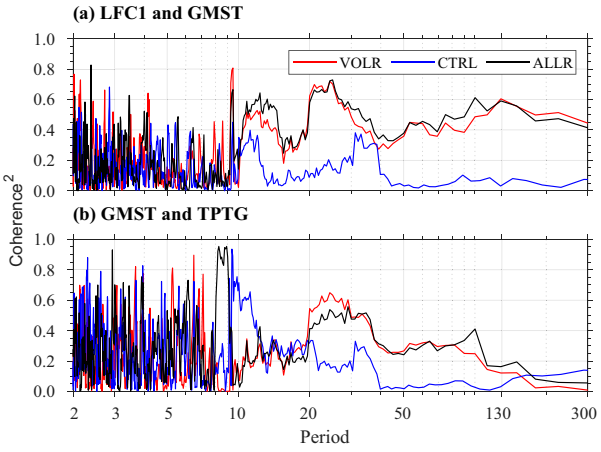

FIG. 6. (a) Squared coherence between LFC1 and GMST, both from ALLR (black curves) and between LFC1 from ALLR and GMST from VOLR (red curves). Blue curves are the squared coherence between the leading LFC and GMST, both from CTRL. (b) As in (a), but for GMST and TPTG.

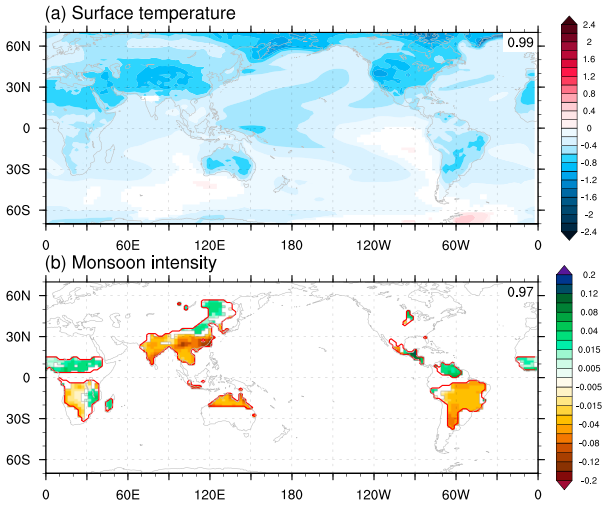

FIG. 7. Composites of significant cool-GMST and weak-TPTG events (22) that occurred simultaneously (<−1.5 standard deviations) over the LM for (a) surface temperature and (b) GLM intensity. Color shading denotes values above the 95% confidence level. The regions outlined by red lines denote GLM areas. The figures in the upper-right corners of the panels indicate the pattern correlation coefficient with the regressed surface temperature (Fig. 2c) and the forced LFP1 (Fig. 2a), respectively.

is evident at decadal to multidecadal time scales, such as 10–15- and 20–30-yr periods, where the squared coherences exceed 50% (black curves). This feature is absent in CTRL (blue curves) and is unidentifiable when using LFC1 from ALLR and GMST from the sensitivity simulations, except for VOLR (red curves). This indicates that the global-scale cooling effect of volcanic eruptions predominantly influences the forced LFC1 variations. The squared coherences between GMST and TPTG, as shown in Fig. 6b, demonstrate that external forcing dominates GMST and TPTG variations for the 20–30-yr period in both ALLR and VOLR, but only within a 10-yr period in CTRL. As previously mentioned (Fig. 5), external forcing can modulate the correlation between GMST and TPTG from negative to positive. Furthermore, TPTG variations usually lag behind GMST changes under externally forced conditions (Brad Adams et al. 2003), indicating that TPTG is a response to GMST changes under some mechanisms (e.g., Bjerknes feedback). This suggests that the global-scale cooling effect of volcanic eruptions could also drive TPTG changes at interdecadal time scales.

To delineate the influence of volcanic activities on surface temperatures and GLM, we identified events over the last millennium where the GMST and TPTG concurrently exhibited marked declines (exceeding −1.5 standard deviations, a threshold selected for statistical robustness). Out of a total of 901 model years in ALLR (12-member ensemble mean), 22 such events were identified, coinciding with the four largest volcanic eruptions (Fig. 2b, red triangles). In contrast, nearly no similar events were observed in CTRL, with only two events out of a total of 1155 model years. These findings suggest that volcanic eruptions could potentially increase the frequency of significant cool GMST and weak TPTG events happening simultaneously.

The results presented here agree with previous studies, suggesting that the primary forced mode of the GLM is influenced by both global-scale cooling and weak TPTG effects, primarily driven by volcanic eruptions, as illustrated in Fig. 7. The composite patterns of surface temperature and the monsoon intensity for the 22 selected events (anomalies relative to the last millennium) have high pattern correlation coefficients with the forced regressed surface temperature (Fig. 2c, $r = 0.99$) and forced LFP1 (Fig. 2a, $r = 0.97$). Additionally, these events occurred consistently with those in VOLR but not in other sensitivity simulations. This finding confirms volcanic eruptions as the predominant external forcing behind the interdecadal variability of the primary forced mode of GLM intensity.

Other external forcings, such as solar irradiation, land use, and land cover, also play crucial roles in climate dynamics. While large-scale land use and land changes may have had significant impacts on regional monsoon impacts (Quesada et al. 2017), they changed little in most of the regions over the last millennium (Wang et al. 2023). Solar irradiation, akin to volcanic activity, modulates the TPTG evolution, thereby affecting monsoon climate on multidecadal to centennial time scales (Sun et al. 2022). Despite these influences, the CESM-LME experiments in this study do not reveal a clear solar forcing signal within the leading forced GLM variations, possibly due to relatively small solar variation inputs. However, evidence from previous research employing CESM driven by strong solar forcing suggests that volcanic influences may eclipse solar activity in governing decadal to multidecadal time-scale GMST variations (Wang et al. 2019).

In conclusion, volcanic eruptions are the predominant external forcing that affects the GMST and TPTG. These factors together critically shape the spatiotemporal variations of

the leading forced mode of GLM intensity on interdecadal time scales throughout the last millennium. This assertion aligns with existing literature that illustrates volcanic activity's direct and indirect influences on the monsoon climate, namely, through aerosol-induced cooling and by fostering El Niño–like states (TPTG pattern effects). Notably, the occurrence of such conditions following volcanic eruptions has been documented in prior works, especially the tropical volcanic eruptions (e.g., Brad Adams et al. 2003; Cobb et al. 2003; Li et al. 2013; Stoffel et al. 2015; Khodri et al. 2017; Sun et al. 2019). These processes have been recognized as significant independent modulators of GLM. While the detailed physical mechanisms related to the influence of volcanic eruptions on tropical Pacific surface temperature changes have been proposed and warrant further investigation, they are beyond the scope of this study. Furthermore, TPTG patterns in response to composites of selected volcanic eruption events (Zuo et al. 2018, 2019), depending on erupt latitudes and preexisting TPTG conditions, suggest a complex interplay in how GLM intensity responds to volcanic eruptions. Nevertheless, these research findings do not contradict our results, illuminating the primary patterns and evolution of GLM in response to the continuous eruptions at interdecadal time scales over the last millennium.

4. Summary and concluding remarks

The present work was devoted to the variation of global land monsoon (GLM) on interdecadal time scales over the last millennium (AD 950–1850), a period characterized by significant natural external forcings. While internal variability was generally found important for this recent period of Earth's history, natural external forcings, such as solar forcing and volcanic eruptions, do exert substantial influences on GLM variation. The multirealization approach in the CESM-LME dataset, together with the sensitivity experiments run under conditions of individual forcings, allows us to isolate the signal. The emergence of the signal was also facilitated by low-frequency component analysis (LFCA), a powerful tool to extract low-frequency components in the complex climate system. Our key findings are as follows:

1) The primary forced mode of GLM, representing 19% of the total variance, exhibits consistent features over South Asia, the southern part of East Asia, North Australia, South America, and western South Africa, but it shows contrasted features in other monsoon regions. Such a pattern is the response to the combined effects of global-scale cooling [measured by the global mean surface temperature (GMST)] and weaker Walker circulation over the tropical Pacific (measured by the TPTG).
2) A composite analysis further reveals that the general global cooling reduces atmospheric moisture and weakens the GLM intensity in most monsoon regions, except for the southern Asian monsoon regions, which enhance the monsoon intensity. The weak TPTG primarily affects the atmospheric circulation, akin to the effects of an El Niño–like pattern, significantly concerning the weakening monsoon intensity over almost all monsoon regions.
3) Although the weak TPTG is primarily associated with the GLM intensity in both control (CTRL) and all-forcing run (ALLR) simulations, the time scale of its action differs, and the final effect is also different. In CTRL, a negative correlation exists between TPTG and GMST, with TPTG solely driving the spatiotemporal variation of GLM. In ALLR, however, natural external forcings trigger interdecadal TPTG variation that is positively correlated with the ensemble mean GMST, the two jointly modulating the GLM intensity variation. GMST and TPTG together explain 75% of the total variance in the primary forced mode of GLM, with individual contributions of 29% from GMST and 46% from TPTG.
4) The sensitivity simulations, performed with single external forcings individually applied, allow us to conclude further that volcanic eruptions are the primary external forcing leading to the global cooling (GMST) and concurrent interdecadal TPTG pattern. They jointly modulate the primary forced GLM variation over the last millennium, including its spatial pattern and temporal evolution.

Finally, it is important to recognize that our conclusions are based on a single model, which introduces potential model dependence on the results. As computational resources expand, the future will likely see an increase in large ensemble experiments that can corroborate and refine our comprehension of how natural external forcings shape interdecadal GLM variations. The role of natural external forcings in projecting interdecadal monsoon variations must be considered. Recent volcanic activity, for instance, has been observed to perturb monsoon precipitation patterns over several years—deviations that were not anticipated in prior climate projections (Zuo et al. 2022). Therefore, future climate simulation frameworks should integrate natural external forcings to narrow uncertainties in hydroclimatic prediction, especially in scenarios akin to the frequent volcanic activity observed in the last millennium.

Acknowledgments. This study was supported by the Key Special Funding for the National Key R&D Plan (2023YFE0103500) and the National Natural Science Foundation of China (41901095 and 42101044). We acknowledge Wills et al. (2018) for providing the LFCA codes. We thank all CESM-LME members for producing and making their model outputs available. Calculations and plotting have primarily been performed using the NCAR Command Language (NCL) software (NCAR, Boulder, Colorado) and Climate Data Operators (CDO); see https://code.mpimet.mpg.de/projects/cdo.

Data availability statement. Reanalysis precipitation data are from the Global Precipitation Climatology Project. For more information about data availability, please see https://climatedataguide.ucar.edu/climate-data/gpcp-monthly-global-precipitation-climatology-project. CESM-LME datasets are available from https://www.cesm.ucar.edu/community-projects/lme. LFCA codes used in this study can be downloaded from https://github.com/rcjwills/lfca.

REFERENCES

Adler, R. F., and Coauthors, 2003: The version-2 Global Precipitation Climatology Project (GPCP) monthly precipitation analysis (1979–present). *J. Hydrometeor.*, **4**, 1147–1167, https://doi.org/10.1175/1525-7541(2003)004<1147:TVGPCP>2.0.CO;2.

Allen, M. R., and W. J. Ingram, 2002: Constraints on future changes in climate and the hydrologic cycle. *Nature*, **419**, 224–232, https://doi.org/10.1038/nature01092.

Bauer, E., M. Claussen, V. Brovkin, and A. Huenerbein, 2003: Assessing climate forcings of the Earth system for the past millennium. *Geophys. Res. Lett.*, **30**, 1276, https://doi.org/10.1029/2002GL016639.

Brad Adams, J., M. E. Mann, and C. M. Ammann, 2003: Proxy evidence for an El Niño-like response to volcanic forcing. *Nature*, **426**, 274–278, https://doi.org/10.1038/nature02101.

Cane, M. A., A. C. Clement, A. Kaplan, Y. Kushnir, D. Pozdnyakov, R. Seager, S. E. Zebiak, and R. Murtugudde, 1997: Twentieth-century sea surface temperature trends. *Science*, **275**, 957–960, https://doi.org/10.1126/science.275.5302.957.

Chen, K., L. Ning, Z. Liu, J. Liu, M. Yan, W. Sun, L. Li, and Z. Shi, 2022: Modulating and resetting impacts of different volcanic eruptions on North Atlantic SST variations. *J. Geophys. Res. Atmos.*, **127**, e2021JD036246, https://doi.org/10.1029/2021JD036246.

Chen, Z., T. Zhou, L. Zhang, X. Chen, W. Zhang, and J. Jiang, 2020: Global land monsoon precipitation changes in CMIP6 projections. *Geophys. Res. Lett.*, **47**, e2019GL086902, https://doi.org/10.1029/2019GL086902.

Cheung, A. H., M. E. Mann, B. A. Steinman, L. M. Frankcombe, M. H. England, and S. K. Miller, 2017: Comparison of low-frequency internal climate variability in CMIP5 models and observations. *J. Climate*, **30**, 4763–4776, https://doi.org/10.1175/JCLI-D-16-0712.1.

Clement, A. C., R. Seager, M. A. Cane, and S. E. Zebiak, 1996: An ocean dynamical thermostat. *J. Climate*, **9**, 2190–2196, https://doi.org/10.1175/1520-0442(1996)009<2190:AODT>2.0.CO;2.

Cobb, K. M., C. D. Charles, H. Cheng, and R. L. Edwards, 2003: El Niño/Southern Oscillation and tropical Pacific climate during the last millennium. *Nature*, **424**, 271–276, https://doi.org/10.1038/nature01779.

Crowley, T. J., 2000: Causes of climate change over the past 1000 years. *Science*, **289**, 270–277, https://doi.org/10.1126/science.289.5477.270.

Deser, C., R. Knutti, S. Solomon, and A. S. Phillips, 2012: Communication of the role of natural variability in future North American climate. *Nat. Climate Change*, **2**, 775–779, https://doi.org/10.1038/nclimate1562.

——, A. S. Phillips, M. A. Alexander, and B. V. Smoliak, 2014: Projecting North American climate over the next 50 years: Uncertainty due to internal variability. *J. Climate*, **27**, 2271–2296, https://doi.org/10.1175/JCLI-D-13-00451.1.

He, C., and W. Zhou, 2020: Different enhancement of the East Asian summer monsoon under global warming and interglacial epochs simulated by CMIP6 models: Role of the subtropical high. *J. Climate*, **33**, 9721–9733, https://doi.org/10.1175/JCLI-D-20-0304.1.

Hegerl, G., J. Luterbacher, F. González-Rouco, S. F. B. Tett, T. Crowley, and E. Xoplaki, 2011: Influence of human and natural forcing on European seasonal temperatures. *Nat. Geosci.*, **4**, 99–103, https://doi.org/10.1038/ngeo1057.

Hsu, P.-C., T. Li, J.-J. Luo, H. Murakami, A. Kitoh, and M. Zhao, 2012: Increase of global monsoon area and precipitation under global warming: A robust signal? *Geophys. Res. Lett.*, **39**, L06701, https://doi.org/10.1029/2012GL051037.

——, ——, H. Murakami, and A. Kitoh, 2013: Future change of the global monsoon revealed from 19 CMIP5 models. *J. Geophys. Res. Atmos.*, **118**, 1247–1260, https://doi.org/10.1002/jgrd.50145.

Huang, P., S.-P. Xie, K. Hu, G. Huang, and R. Huang, 2013: Patterns of the seasonal response of tropical rainfall to global warming. *Nat. Geosci.*, **6**, 357–361, https://doi.org/10.1038/ngeo1792.

Kay, J. E., and Coauthors, 2015: The Community Earth System Model (CESM) large ensemble project: A community resource for studying climate change in the presence of internal climate variability. *Bull. Amer. Meteor. Soc.*, **96**, 1333–1349, https://doi.org/10.1175/BAMS-D-13-00255.1.

Khodri, M., and Coauthors, 2017: Tropical explosive volcanic eruptions can trigger El Niño by cooling tropical Africa. *Nat. Commun.*, **8**, 778, https://doi.org/10.1038/s41467-017-00755-6.

Kitoh, A., H. Endo, K. Krishna Kumar, I. F. A. Cavalcanti, P. Goswami, and T. Zhou, 2013: Monsoons in a changing world: A regional perspective in a global context. *J. Geophys. Res. Atmos.*, **118**, 3053–3065, https://doi.org/10.1002/jgrd.50258.

Lee, J.-Y., and B. Wang, 2014: Future change of global monsoon in the CMIP5. *Climate Dyn.*, **42**, 101–119, https://doi.org/10.1007/s00382-012-1564-0.

Li, J., and Coauthors, 2013: El Niño modulations over the past seven centuries. *Nat. Climate Change*, **3**, 822–826, https://doi.org/10.1038/nclimate1936.

Liu, F., J. Chai, B. Wang, J. Liu, X. Zhang, and Z. Wang, 2016: Global monsoon precipitation responses to large volcanic eruptions. *Sci. Rep.*, **6**, 24331, https://doi.org/10.1038/srep24331.

Liu, J., B. Wang, Q. Ding, X. Kuang, W. Soon, and E. Zorita, 2009: Centennial variations of the global monsoon precipitation in the last millennium: Results from ECHO-G model. *J. Climate*, **22**, 2356–2371, https://doi.org/10.1175/2008JCLI2353.1.

——, ——, S.-Y. Yim, J.-Y. Lee, J.-G. Jhun, and K.-J. Ha, 2012: What drives the global summer monsoon over the past millennium? *Climate Dyn.*, **39**, 1063–1072, https://doi.org/10.1007/s00382-012-1360-x.

——, ——, M. A. Cane, S.-Y. Yim, and J.-Y. Lee, 2013: Divergent global precipitation changes induced by natural versus anthropogenic forcing. *Nature*, **493**, 656–659, https://doi.org/10.1038/nature11784.

Man, W., and T. Zhou, 2014: Regional-scale surface air temperature and East Asian summer monsoon changes during the last millennium simulated by the FGOALS-gl climate system model. *Adv. Atmos. Sci.*, **31**, 765–778, https://doi.org/10.1007/s00376-013-3123-y.

Mann, M. E., and Coauthors, 2009: Global signatures and dynamical origins of the little ice age and medieval climate anomaly. *Science*, **326**, 1256–1260, https://doi.org/10.1126/science.1177303.

——, S. K. Miller, S. Rahmstorf, B. A. Steinman, and M. Tingley, 2017: Record temperature streak bears anthropogenic fingerprint. *Geophys. Res. Lett.*, **44**, 7936–7944, https://doi.org/10.1002/2017GL074056.

Miller, G. H., and Coauthors, 2012: Abrupt onset of the little ice age triggered by volcanism and sustained by sea-ice/ocean feedbacks. *Geophys. Res. Lett.*, **39**, L02708, https://doi.org/10.1029/2011GL050168.

Otto-Bliesner, B. L., and Coauthors, 2016: Climate variability and change since 850 CE: An ensemble approach with the

Community Earth System Model. *Bull. Amer. Meteor. Soc.*, **97**, 735–754, https://doi.org/10.1175/BAMS-D-14-00233.1.

Pausata, F. S. R., and S. J. Camargo, 2019: Tropical cyclone activity affected by volcanically induced ITCZ shifts. *Proc. Natl. Acad. Sci. USA*, **116**, 7732–7737, https://doi.org/10.1073/pnas.1900777116.

Piao, J., W. Chen, S. Chen, H. Gong, Z. Wang, and X. Lan, 2023: How well do CMIP6 models simulate the climatological northern boundary of the East Asian summer monsoon? *Global Planet. Change*, **221**, 104034, https://doi.org/10.1016/j.gloplacha.2023.104034.

Polson, D., M. Bollasina, G. C. Hegerl, and L. J. Wilcox, 2014: Decreased monsoon precipitation in the Northern Hemisphere due to anthropogenic aerosols. *Geophys. Res. Lett.*, **41**, 6023–6029, https://doi.org/10.1002/2014GL060811.

Quesada, B., N. Devaraju, N. de Noblet-Ducoudré, and A. Arneth, 2017: Reduction of monsoon rainfall in response to past and future land use and land cover changes. *Geophys. Res. Lett.*, **44**, 1041–1050, https://doi.org/10.1002/2016GL070663.

Robock, A., 2000: Volcanic eruptions and climate. *Rev. Geophys.*, **38**, 191–219, https://doi.org/10.1029/1998RG000054.

Rotstayn, L. D., and U. Lohmann, 2002: Tropical rainfall trends and the indirect aerosol effect. *J. Climate*, **15**, 2103–2116, https://doi.org/10.1175/1520-0442(2002)015<2103:TRTATI>2.0.CO;2.

Steinman, B. A., M. E. Mann, and S. K. Miller, 2015: Atlantic and Pacific multidecadal oscillations and Northern Hemisphere temperatures. *Science*, **347**, 988–991, https://doi.org/10.1126/science.1257856.

Stoffel, M., and Coauthors, 2015: Estimates of volcanic-induced cooling in the Northern Hemisphere over the past 1,500 years. *Nat. Geosci.*, **8**, 784–788, https://doi.org/10.1038/ngeo2526.

Sun, W., J. Liu, B. Wang, D. Chen, F. Liu, Z. Wang, L. Ning, and M. Chen, 2019: A "La Niña-like" state occurring in the second year after large tropical volcanic eruptions during the past 1500 years. *Climate Dyn.*, **52**, 7495–7509, https://doi.org/10.1007/s00382-018-4163-x.

——, ——, ——, ——, L. Wan, and J. Wang, 2022: Holocene multi-centennial variations of the Asian summer monsoon triggered by solar activity. *Geophys. Res. Lett.*, **49**, e2022GL098625, https://doi.org/10.1029/2022GL098625.

Tian, B., and X. Dong, 2020: The double-ITCZ bias in CMIP3, CMIP5, and CMIP6 models based on annual mean precipitation. *Geophys. Res. Lett.*, **47**, e2020GL087232, https://doi.org/10.1029/2020GL087232.

Trenberth, K. E., D. P. Stepaniak, and J. M. Caron, 2000: The global monsoon as seen through the divergent atmospheric circulation. *J. Climate*, **13**, 3969–3993, https://doi.org/10.1175/1520-0442(2000)013<3969:TGMAST>2.0.CO;2.

Wang, B., and Q. Ding, 2006: Changes in global monsoon precipitation over the past 56 years. *Geophys. Res. Lett.*, **33**, L06711, https://doi.org/10.1029/2005GL025347.

——, and ——, 2008: Global monsoon: Dominant mode of annual variation in the tropics. *Dyn. Atmos. Oceans*, **44**, 165–183, https://doi.org/10.1016/j.dynatmoce.2007.05.002.

——, R. Wu, and T. Li, 2003: Atmosphere–warm ocean interaction and its impacts on Asian–Australian monsoon variation. *J. Climate*, **16**, 1195–1211, https://doi.org/10.1175/1520-0442(2003)16<1195:AOIAII>2.0.CO;2.

——, H.-J. Kim, K. Kikuchi, and A. Kitoh, 2011: Diagnostic metrics for evaluation of annual and diurnal cycles. *Climate Dyn.*, **37**, 941–955, https://doi.org/10.1007/s00382-010-0877-0.

——, J. Liu, H.-J. Kim, P. J. Webster, and S.-Y. Yim, 2012: Recent change of the global monsoon precipitation (1979–2008). *Climate Dyn.*, **39**, 1123–1135, https://doi.org/10.1007/s00382-011-1266-z.

——, ——, ——, ——, ——, and B. Xiang, 2013: Northern Hemisphere summer monsoon intensified by mega-El Niño/Southern Oscillation and Atlantic multidecadal oscillation. *Proc. Natl. Acad. Sci. USA*, **110**, 5347–5352, https://doi.org/10.1073/pnas.1219405110.

——, C. Jin, and J. Liu, 2020: Understanding future change of global monsoons projected by CMIP6 models. *J. Climate*, **33**, 6471–6489, https://doi.org/10.1175/JCLI-D-19-0993.1.

Wang, G., W. Cai, B. Gan, L. Wu, A. Santoso, X. Lin, Z. Chen, and M. J. McPhaden, 2017: Continued increase of extreme El Niño frequency long after 1.5°C warming stabilization. *Nat. Climate Change*, **7**, 568–572, https://doi.org/10.1038/nclimate3351.

Wang, P. X., B. Wang, H. Cheng, J. Fasullo, Z. T. Guo, T. Kiefer, and Z. Y. Liu, 2014: The global monsoon across timescales: Coherent variability of regional monsoons. *Climate Past*, **10**, 2007–2052, https://doi.org/10.5194/cp-10-2007-2014.

——, ——, ——, ——, Z. Guo, T. Kiefer, and Z. Liu, 2017: The global monsoon across time scales: Mechanisms and outstanding issues. *Earth-Sci. Rev.*, **174**, 84–121, https://doi.org/10.1016/j.earscirev.2017.07.006.

Wang, Z., J. Wang, and S. Zhang, 2019: Variations of the global annual mean surface temperature during the past 2000 years: Results from the CESM1. *Theor. Appl. Climatol.*, **137**, 2877–2887, https://doi.org/10.1007/s00704-019-02775-2.

——, ——, J. Jia, and J. Liu, 2021: The forced response of Asian summer monsoon precipitation during the past 1500 years based on the CESM (in Chinese). *Acta Geogr. Sin.*, **76**, 550–565, https://doi.org/10.11821/dlxb202103005.

——, ——, ——, X. Shi, S. Wang, and C. Pan, 2022: Detection and attribution of summer temperature changes in China during the last millennium. *Int. J. Climatol.*, **42**, 6384–6402, https://doi.org/10.1002/joc.7595.

——, ——, X. Shi, J. Jia, and M. Yan, 2023: Causes of decadal distributions of Indian summer monsoon rainfall during the last 1500 years. *J. Quat. Sci.*, **38**, 243–257, https://doi.org/10.1002/jqs.3469.

Webster, P. J., and S. Yang, 1992: Monsoon and ENSO: Selectively interactive systems. *Quart. J Roy. Meteor. Soc.*, **118**, 877–926, https://doi.org/10.1002/qj.49711850705.

Williams, K. D., A. Jones, D. L. Roberts, C. A. Senior, and M. J. Woodage, 2001: The response of the climate system to the indirect effects of anthropogenic sulfate aerosol. *Climate Dyn.*, **17**, 845–856, https://doi.org/10.1007/s003820100150.

Wills, R. C., T. Schneider, J. M. Wallace, D. S. Battisti, and D. L. Hartmann, 2018: Disentangling global warming, multidecadal variability, and El Niño in Pacific temperatures. *Geophys. Res. Lett.*, **45**, 2487–2496, https://doi.org/10.1002/2017GL076327.

Wills, R. C. J., D. S. Battisti, K. C. Armour, T. Schneider, and C. Deser, 2020: Pattern recognition methods to separate forced responses from internal variability in climate model ensembles and observations. *J. Climate*, **33**, 8693–8719, https://doi.org/10.1175/JCLI-D-19-0855.1.

Xue, J., and Coauthors, 2023: The combined influences of solar radiation and PDO on precipitation over Eastern China during the last millennium. *Climate Dyn.*, **60**, 1137–1150, https://doi.org/10.1007/s00382-022-06372-4.

Zeng, J., and Q. Zhang, 2020: The trends in land surface heat fluxes over global monsoon domains and their responses to

monsoon and precipitation. *Sci. Rep.*, **10**, 5762, https://doi.org/10.1038/s41598-020-62467-0.

Zhang, L., and T. Zhou, 2011: An assessment of monsoon precipitation changes during 1901–2001. *Climate Dyn.*, **37**, 279–296, https://doi.org/10.1007/s00382-011-0993-5.

Zhao, Y., Z. Zheng, R. Zhi, G. Feng, and J. Cheng, 2022: The zonal gradient structures of wintertime SST anomalies in the equatorial Pacific and their connection to the walker circulation. *Climate Dyn.*, **58**, 841–859, https://doi.org/10.1007/s00382-021-05939-x.

Zinke, J., S. A. Browning, A. Hoell, and I. D. Goodwin, 2021: The west Pacific gradient tracks ENSO and zonal Pacific sea surface temperature gradient during the last millennium. *Sci. Rep.*, **11**, 20395, https://doi.org/10.1038/s41598-021-99738-3.

Zuo, M., W. Man, T. Zhou, and Z. Guo, 2018: Different impacts of northern, tropical, and southern volcanic eruptions on the tropical Pacific SST in the last millennium. *J. Climate*, **31**, 6729–6744, https://doi.org/10.1175/JCLI-D-17-0571.1.

——, T. Zhou, and W. Man, 2019: Hydroclimate responses over global monsoon regions following volcanic eruptions at different latitudes. *J. Climate*, **32**, 4367–4385, https://doi.org/10.1175/JCLI-D-18-0707.1.

——, W. Man, and T. Zhou, 2021: Dependence of global monsoon response to volcanic eruptions on the background oceanic states. *J. Climate*, **34**, 8273–8289, https://doi.org/10.1175/JCLI-D-20-0891.1.

——, T. Zhou, W. Man, X. Chen, J. Liu, F. Liu, and C. Gao, 2022: Volcanoes and Climate: Sizing up the impact of the recent Hunga Tonga-Hunga Ha'apai volcanic eruption from a historical perspective. *Adv. Atmos. Sci.*, **39**, 1986–1993, https://doi.org/10.1007/s00376-022-2034-1.

——, ——, and ——, 2023: Response of summer precipitation over the Tibetan Plateau to large tropical volcanic eruptions in the last millennium. *Climate Dyn.*, **60**, 3121–3138, https://doi.org/10.1007/s00382-022-06463-2.